PLOS PATHOGENS

RESEARCH ARTICLE

A natural mutation between SARS-CoV-2 and SARS-CoV determines neutralization by a cross-reactive antibody

Nicholas C. Wu[1,2☯], Meng Yuan[3☯], Sandhya Bangaru[3☯], Deli Huang[4☯], Xueyong Zhu[3], Chang-Chun D. Lee[3], Hannah L. Turner[3], Linghang Peng[4], Linlin Yang[4], Dennis R. Burton[4,5,6,7], David Nemazee[4], Andrew B. Ward[3,5,6]*, Ian A. Wilson[3,5,6,8]*

1 Department of Biochemistry, University of Illinois at Urbana-Champaign, Urbana, IL, United States of America, **2** Carl R. Woese Institute for Genomic Biology, University of Illinois at Urbana-Champaign, Urbana, IL, United States of America, **3** Department of Integrative Structural and Computational Biology, The Scripps Research Institute, La Jolla, CA, United States of America, **4** Department of Immunology and Microbiology, The Scripps Research Institute, La Jolla, CA, United States of America, **5** IAVI Neutralizing Antibody Center, The Scripps Research Institute, La Jolla, CA, United States of America, **6** Consortium for HIV/AIDS Vaccine Development (CHAVD), The Scripps Research Institute, La Jolla, CA, United States of America, **7** Ragon Institute of Massachusetts General Hospital, Massachusetts Institute of Technology, and Harvard University, Cambridge, MA, United States of America, **8** The Skaggs Institute for Chemical Biology, The Scripps Research Institute, La Jolla, CA, United States of America

☯ These authors contributed equally to this work.
* andrew@scripps.edu (ABW); wilson@scripps.edu (IAW)

Citation: Wu NC, Yuan M, Bangaru S, Huang D, Zhu X, Lee C-CD, et al. (2020) A natural mutation between SARS-CoV-2 and SARS-CoV determines neutralization by a cross-reactive antibody. PLoS Pathog 16(12): e1009089. https://doi.org/10.1371/journal.ppat.1009089

Editor: Michael S. Diamond, Washington University School of Medicine, UNITED STATES

Received: September 20, 2020

Accepted: October 21, 2020

Published: December 4, 2020

Data Availability Statement: The X-ray coordinates and structure factors have been deposited to the RCSB Protein Data Bank under accession code: 7JN5. The EM maps have been deposited in the Electron Microscopy Data Bank (EMDB) under accession codes: EMD-22858 (nsEM, one bound), EMD-22859 (nsEM, two bound), EMD-22860 (nsEM, three bound), EMD-22861 (cryo-EM, class 1), EMD-22862 (cryo-EM, class 2), EMD-22863 (cryo-EM, class 3), and EMD-22864 (cryo-EM, class 4).

Abstract

Epitopes that are conserved among SARS-like coronaviruses are attractive targets for design of cross-reactive vaccines and therapeutics. CR3022 is a SARS-CoV neutralizing antibody to a highly conserved epitope on the receptor binding domain (RBD) on the spike protein that is able to cross-react with SARS-CoV-2, but with lower affinity. Using x-ray crystallography, mutagenesis, and binding experiments, we illustrate that of four amino acid differences in the CR3022 epitope between SARS-CoV-2 and SARS-CoV, a single mutation P384A fully determines the affinity difference. CR3022 does not neutralize SARS-CoV-2, but the increased affinity to SARS-CoV-2 P384A mutant now enables neutralization with a similar potency to SARS-CoV. We further investigated CR3022 interaction with the SARS-CoV spike protein by negative-stain EM and cryo-EM. Three CR3022 Fabs bind per trimer with the RBD observed in different up-conformations due to considerable flexibility of the RBD. In one of these conformations, quaternary interactions are made by CR3022 to the N-terminal domain (NTD) of an adjacent subunit. Overall, this study provides insights into antigenic variation and potential cross-neutralizing epitopes on SARS-like viruses.

Author summary

The ongoing COVID-19 pandemic is caused by SARS-CoV-2. Due to the genetic similarity of SARS-CoV-2 and SARS-CoV, which caused an epidemic in 2003, a few of the

Funding: This work was supported by NIH R00 AI139445 (N.C.W.), NIH R01 AI073148 (D.N.), the Bill and Melinda Gates Foundation OPP1170236 (D.R.B., A.B.W. and I.A.W.) and NIH CHAVD UM1 AI44462 (D.R.B., A.B.W. and I.A.W.). Use of the SSRL, SLAC National Accelerator Laboratory, is supported by the U.S. Department of Energy, Office of Science, Office of Basic Energy Sciences under Contract No. DE-AC02–76SF00515. The SSRL Structural Molecular Biology Program is supported by the DOE Office of Biological and Environmental Research, and by the National Institutes of Health, National Institute of General Medical Sciences (including P41GM103393). The funders had no role in study design, data collection and analysis, decision to publish, or preparation of the manuscript.

Competing interests: The authors have declared that no competing interests exist.

SARS-CoV antibodies have now been found to also cross-react with SARS-CoV-2. One such antibody is CR3022, which was isolated from a convalescent SARS patient 14 years ago. However, the 100-fold lower binding to SARS-CoV-2 does not enable neutralization of SARS-CoV-2 compared to SARS-CoV. This study shows that one (P384A) of the four mutational differences in the CR3022 epitope between SARS-CoV and SARS-COV-2 fully accounts for the differences in CR3022 binding affinity and neutralization. These findings advance our understanding of antibody cross-reactivity among SARS-like CoVs with implications for vaccine and therapeutic design.

Introduction

The ongoing COVID-19 pandemic, which is caused by the new coronavirus SARS-CoV-2, continues to escalate. Investigating the immunogenicity and antigenicity of SARS-CoV-2 is germane to vaccine and therapeutic development. The major antigen of coronavirus is the spike (S) glycoprotein, which is expressed as a homotrimer on the virus surface. Since the S protein is essential for virus entry through engaging the host receptor and mediating virus-host membrane fusion, many antibodies to the S protein are neutralizing [1–12]. The S proteins of SARS-CoV-2 and SARS-CoV, which caused a global outbreak in 2003, have an amino-acid sequence identity of around 77% [13] that leads to differences in antigenicity in serology studies [14,15]. Although a few monoclonal antibodies have been discovered that can cross-neutralize SARS-CoV and SARS-CoV-2 [6,7,16,17], they seem to be relatively rare in COVID-19 patients [1,3,4,14]. Thus, the molecular determinants that define the antigenic differences and similarities between SARS-CoV-2 and SARS-CoV need further exploration.

CR3022 was previously isolated from a SARS survivor and neutralizes SARS-CoV [18], CR3022 was recently found to also be a cross-reactive antibody that can bind to both SARS--CoV-2 and SARS-CoV [19]. Our recent crystal structure demonstrated that CR3022 targets a highly conserved cryptic epitope on the receptor binding domain (RBD) of the S protein [20]. The CR3022 epitope is exposed only when the RBD is in the "up" but not the "down" conformation on the S protein [20]. A few SARS-CoV-2 antibodies from COVID-19 patients have also recently been shown to target the CR3022 epitope [12,17,21], suggesting that it is an important site of vulnerability for the antibody response in SARS-CoV-2 infection. Out of 28 residues in the CR3022 epitope, 24 are conserved between SARS-CoV-2 and SARS-CoV, explaining the cross-reactive binding of CR3022. However, CR3022 has a higher affinity to SARS-CoV than to SARS-CoV-2 (>100-fold difference), and can neutralize SARS-CoV, but not SARS-CoV-2, in a live virus neutralization assay [20]. Therefore, CR3022 provides a good case study to probe antigenic variation between SARS-CoV-2 and SARS-CoV and the effects on antibody cross-neutralization.

We therefore aimed to dissect the molecular basis underlying the difference in binding affinity and neutralization potency of CR3022 to SARS-CoV-2 and SARS-CoV. The crystal structure of SARS-CoV RBD in complex with CR3022 was determined to compare with the corresponding SARS-CoV-2 RBD structure [20]. In combination of mutagenesis and binding experiments, we demonstrate that a single amino-acid difference at residue 384 (SARS-CoV-2 numbering) between the RBDs of SARS-CoV-2 and SARS-CoV can fully explain the affinity difference with CR3022. Moreover, CR3022 is now able to neutralize SARS-CoV-2 P384A with a similar potency to SARS-CoV. We further investigated the molecular recognition of CR3022 to the SARS-CoV-2 spike protein by electron microscopy and found that rotational flexibility of the RBD resulted in antibody binding to different variants of up-conformations of

the RBD relative to the spike trimer. Our findings validate the CR3022 epitope as a major site of vulnerability for a cross-neutralizing antibody response. Throughout this study, residues on RBD are numbered according to SARS-CoV-2 numbering unless otherwise stated.

Results

P384A increases binding affinity of SARS-CoV-2 RBD to CR3022

The epitopes of CR3022 in SARS-CoV-2 and SARS-CoV differ by four residues. We aimed to determine whether amino-acid variants in these four non-conserved residues influence the binding affinity of CR3022 to RBD. Four SARS-CoV-2 RBD mutants, namely A372T, P384A, T430M, and H519N (SARS-CoV-2 numbering), were recombinantly expressed and examined (Fig 1A). These mutants converted the amino-acid sequence of the CR3022 epitope in the SARS-CoV-2 RBD to that of SARS-CoV at each of the four non-conserved residues. While binding of CR3022 mutants A372T (K_D = 66 nM), T430M (K_D = 64 nM), and H519N (K_D = 60 nM) was comparable to wild type (WT) SARS-CoV-2 RBD (K_D = 68 nM), binding of CR3022 to the P384A mutant (K_D = 1.4 nM) was greatly increased (Fig 1B), akin now to that with the SARS-CoV RBD (K_D = 1.0 nM) [20]. Thus, the difference in binding affinity of CR3022 to SARS-CoV-2 RBD versus SARS-CoV RBD can be attributed due to a single amino-acid difference at residue 384.

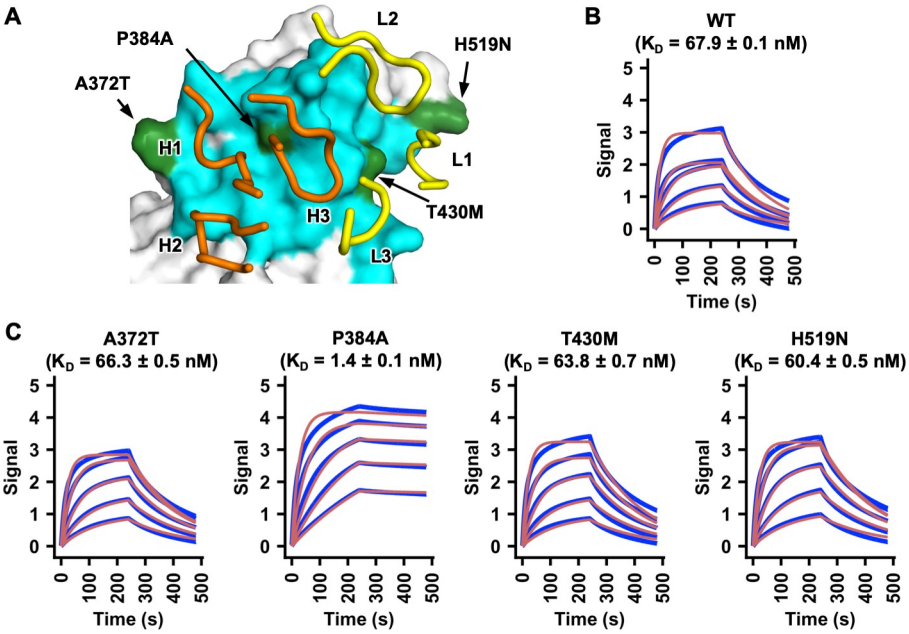

Fig 1. A single P384A substitution increases CR3022 affinity to the SARS-CoV-2 RBD. (A) Epitope residues on SARS-CoV RBD are colored in cyan and green. The CR3022 CDR loops that contact the RBD are shown and labeled. Cyan: epitope residues that are conserved between SARS-CoV-2 and SARS-CoV. Green: epitope residues that are not conserved between SARS-CoV-2 and SARS-CoV. Orange: CR3022 heavy chain. Yellow: CR3022 light chain. **(B-C)** Binding of CR3022 Fab to **(B)** wild-type (WT) SARS-CoV-2 RBD and **(C)** different mutants was measured by biolayer interferometry with RBD loaded on the biosensor and Fab in solution. Y-axis represents the response. Dissociation constants (K_D) for the Fab were obtained using a 1:1 binding model, respectively, which is represented by the red curves. Representative results of two replicates for each experiment are shown. Of note, mammalian cell-expressed RBD was used in the binding experiments in this study, whereas insect cell-expressed RBD was used in our previous study [20]. This difference may explain the slight difference in the K_D of CR3022 Fab to SARS-CoV-2 RBD WT between this study and our previous study [20].

https://doi.org/10.1371/journal.ppat.1009089.g001

CR3022 neutralizes SARS-CoV-2 P384A but not WT

While CR3022 can neutralize SARS-CoV [18,20], multiple groups have shown that it does not neutralize SARS-CoV-2 [3,5,20,22]. One possibility is that the affinity of CR3022 to SARS-CoV-2 RBD is not sufficient to confer neutralizing activity. To test this hypothesis, we compared neutralization of SARS-CoV-2 WT and the P384A mutant by CR3022. Consistent with previous studies [3,5,20,22], CR3022 failed to neutralize SARS-CoV-2 WT (Fig 2). However, CR3022 is now able to neutralize the SARS-CoV-2 P384A mutant at an IC_{50} of 3.2 μg/ml, which is comparable to its neutralizing activity to SARS-CoV (IC_{50} of 5.2 μg/ml). This finding validates the CR3022 epitope as a neutralizing epitope in both SARS-CoV-2 and SARS-CoV, provided that the antibody affinity can surpass a threshold for detection of neutralization.

Previous studies have indicated IgG bivalent binding can play an important role in mediating neutralization of SARS-CoV-2, since the neutralization potency for many antibodies is much greater as an IgG compared to an Fab [21,23]. Subsequently, we also tested the neutralizing activity of CR3022 Fab. Interestingly, the CR3022 Fab neutralized SARS-CoV-2 P384A mutant with an IC_{50} of 4.4 μg/ml, which is similar to that of CR3022 IgG (3.2 μg/ml) (Fig 2). This finding indicates that CR3022, unlike many other SARS-CoV-2 antibodies [21,23], does not act bivalently with the S proteins on the virus surface and, hence, neutralization is related to the Fab binding affinity rather than IgG avidity.

Sequence conservation of residue 384

We then examined the sequence conservation of residue 384 in other SARS-related coronaviruses (SARSr-CoV) strains. Most SARSr-CoV strains have Pro at residue 384, as in SARS-

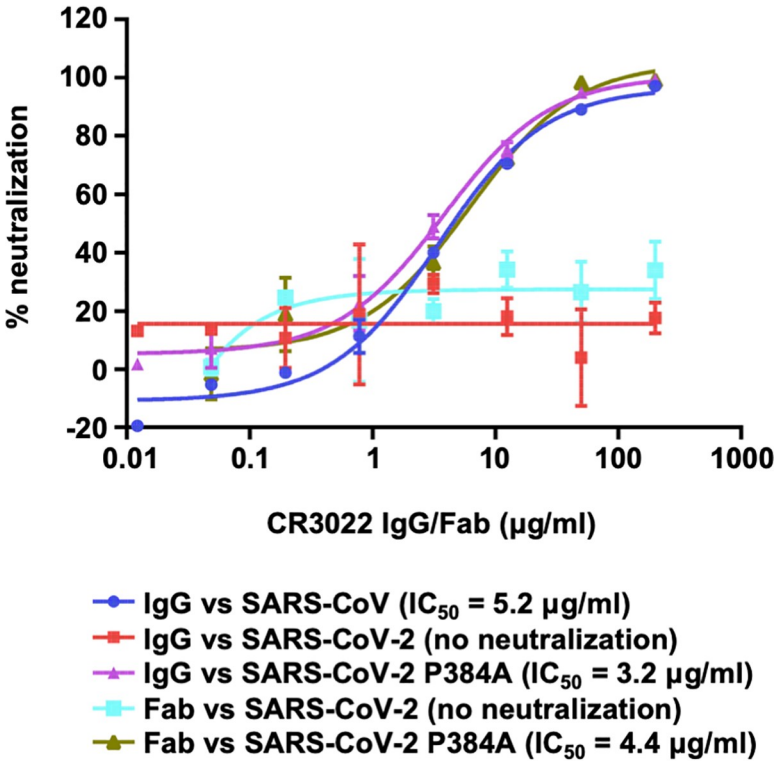

Fig 2. Pseudovirus neutralization assay. The neutralizing activity of CR3022 IgG or Fab to SARS-CoV, SARS-CoV-2, and SARS-CoV-2 P384A mutant was measured in a pseudovirus neutralization assay.

https://doi.org/10.1371/journal.ppat.1009089.g002

CoV-2. Only those strains that are phylogenetically very close to SARS-CoV, such as bat SARSr-CoV WIV1 and bat SARSr-CoV WIV16, have Ala at residue 384 (Figs 3A and S1). Phylogenetic analysis implies that P384A emerged during the evolution of SARSr-CoV in bats (Figs 3A and S1), which is the natural reservoir of SARSr-CoV [24]. However, it is unclear whether the emergence of P384A is due to neutral drift or positive selection in bats or other species. In addition, given that residue 384 is proximal to the S2 domain when the RBD is in the "down" conformation (Fig 3B), whether P384A can modulate the conformational dynamics of the "up and down" configurations of the RBD in the S trimer and influence the viral replication fitness will require additional studies.

Crystal structure reveals the impact of P384A in CR3022 binding

We further determined the x-ray structure of SARS-CoV RBD in complex with CR3022 to 2.7 Å resolution (Figs 4A and S2 and S1 Table). The overall structure of CR3022 in complex with SARS-CoV RBD is similar to that with SARS-CoV-2 RBD [20] (Cα RMSD of 0.5 Å for 343 residues in the RBD and Fab variable domain, cf. Fig S2A and S2B of [20]) (S3 Fig). Nonetheless, the CR3022 elbow angles, which are distant from the antibody-antigen interface, differ in the two structures, as we mutated the elbow region (as described in [25]) of CR3022 to promote crystallization with SARS-CoV RBD. The conserved binding mode of CR3022 to SARS-CoV-2 RBD and SARS-CoV RBD indicates that the difference in binding affinity of CR3022 between SARS-CoV-2 RBD and SARS-CoV RBD is therefore due only to a very subtle structural difference.

To investigate how P384 and A384 lead to differential binding of CR3022, we compared RBD structures from SARS-CoV and SARS-CoV-2 when bound to CR3022. The RBDs have a Cα RMSD of only 0.6 Å (0.7 Å for CR3022 epitope residues). At residue 384, the backbone of SARS-CoV-2 is further from CR3022, as compared to that of SARS-CoV (Fig 4B). This difference in backbone positioning (~1.3 Å shift) affects the interaction of the RBD with CR3022 V_H S96, which is encoded by IGHD3-10 gene segment on CDR H3 [18,20]. While CR3022 V_H S96 forms a hydrogen bond (H-bond) with the T385 side chain in both SARS-CoV-2 RBD and SARS-CoV RBD, it can form a second H-bond with the backbone amide of T385 in

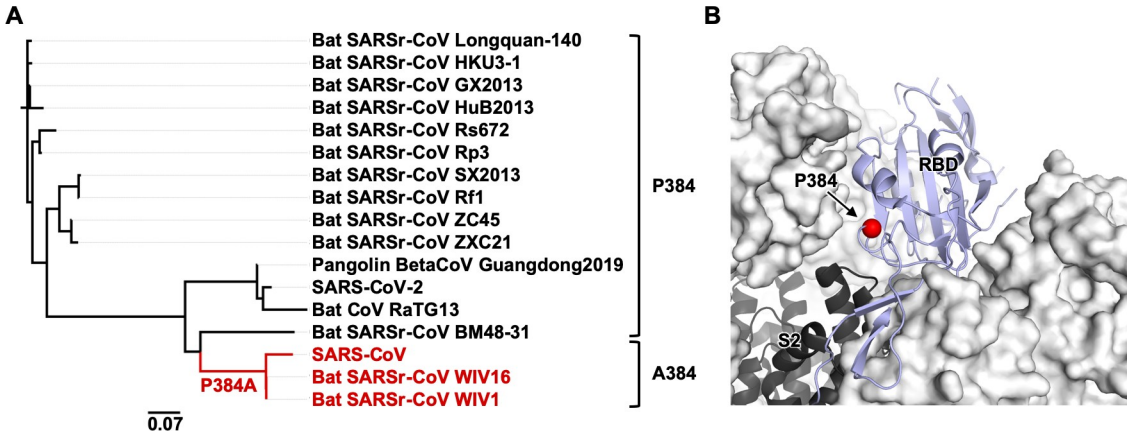

Fig 3. Sequence conservation and location of residue 384. (A) A phylogenetic tree was constructed based on the amino-acid sequences of RBDs from SARS-CoV-2, SARS-CoV, and SARS-related coronavirus (SARSr-CoV) strains. Branches corresponding to strains that have A384 are colored in red on the phylogenetic tree. Scale bar represents 0.07 amino-acid substitutions per position. **(B)** The location of P384 is shown on the SARS-CoV-2 S protein (PDB 6VXX [31]). S1 domain is represented by the white surface and the S2 domain by the black cartoon. The location of residue 384 is indicated by the red sphere on the RBD in the "down" conformation (blue cartoon). CR3022 is not shown in this figure.

https://doi.org/10.1371/journal.ppat.1009089.g003

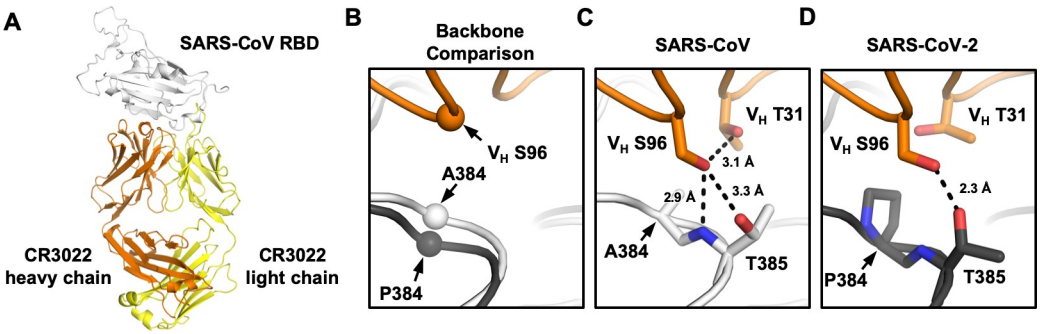

Fig 4. Crystal structure of CR3022 in complex with SARS-CoV RBD. (A) Crystal structure of CR3022 Fab in complex with SARS-CoV RBD. CR3022 heavy chain is colored in orange, CR3022 light chain in yellow, and SARS-CoV-2 RBD in light grey. **(B)** Structures of CR3022 in complex with SARS-CoV-2 RBD and with SARS-CoV RBD were aligned using the CR3022 heavy chain variable domain and the region around residue 384 is shown. Orange: CR3022 heavy chain. White: SARS-CoV RBD. Dark gray: SARS-CoV-2 RBD. The Cαs of S96 on CR3022 heavy chain, A384 on SARS-CoV RBD, and P384 on SARS-CoV-2 RBD are shown in sphere representation. **(C-D)** Interaction between CR3022 and residue 384 on **(C)** SARS-CoV RBD, and **(D)** SARS-CoV-2 RBD. Hydrogen bonds are represented by dashed lines.

https://doi.org/10.1371/journal.ppat.1009089.g004

SARS-CoV RBD (Fig 4C), but not SARS-CoV-2 RBD (Fig 4D). In addition, CR3022 V_H S96 adopts different side-chain rotamers when binding to SARS-CoV-2 and to SARS-CoV. Consequently, V_H S96 can make an intramolecular H-bond with V_H T31 when CR3022 binds to SARS-CoV RBD (Fig 4C), but not to SARS-CoV-2 (Fig 4D). In summary, V_H S96 forms three H-bonds when CR3022 binds to SARS-CoV RBD, as compared to only one when CR3022 binds to SARS-CoV-2 RBD. This observation indicates why binding of CR3022 to the SARS--CoV RBD is energetically more favorable than to the SARS-CoV-2 RBD.

CR3022-bound SARS-CoV S protein exhibits a rare three-up conformation

To understand the binding of CR3022 to the RBD in the context of the homotrimeric S protein, we previously proposed a structural model where CR3022 could only access its epitope on the S protein when at least two RBD are in the "up" conformation and the RBD is rotated relative to its unliganded structure [20]. To further evaluate and expand on this model, negative-stain electron microscopy (nsEM) was performed on CR3022 in complex with a stabilized version of the SARS-CoV homotrimeric S protein (Fig 5A, see Materials and Methods). The 3D nsEM reconstruction revealed that one SARS-CoV S protein could simultaneously bind to three CR3022 Fabs with all three RBDs in the "up" conformation (Fig 5B). Consistent with the structural model that we previously proposed [20], the CR3022-bound RBD was indeed rotated compared to that in the unliganded S protein [26–28], such that, in this conformation, steric hinderance between CR3022 and the N-terminal domain (NTD) is minimized.

While our results here demonstrate that CR3022 Fab could form a stable complex with SARS-CoV S protein in a prefusion conformation, a recent study reported that prefusion SARS-CoV-2 S protein fell apart upon binding to CR3022 Fab as indicated by cryo-EM [29]. It should be noted that the three-up conformation is much more rarely observed than the other RBD conformations (all-down, one-up, and two-up) in SARS-CoV by cryo-EM [26–28], or SARS-CoV-2 by cryo-EM [30–32] and cryo-electron tomography [33,34], and could relate to differences in the stability of S trimers in SARS-CoV versus SARS-CoV-2 when CR3022 is bound. Further studies will be required to investigate whether such a difference between SARS-CoV-2 and SARS-CoV is related to stability differences in the recombinant spike proteins, or to different dynamics of the RBD on the virus or infected cells.

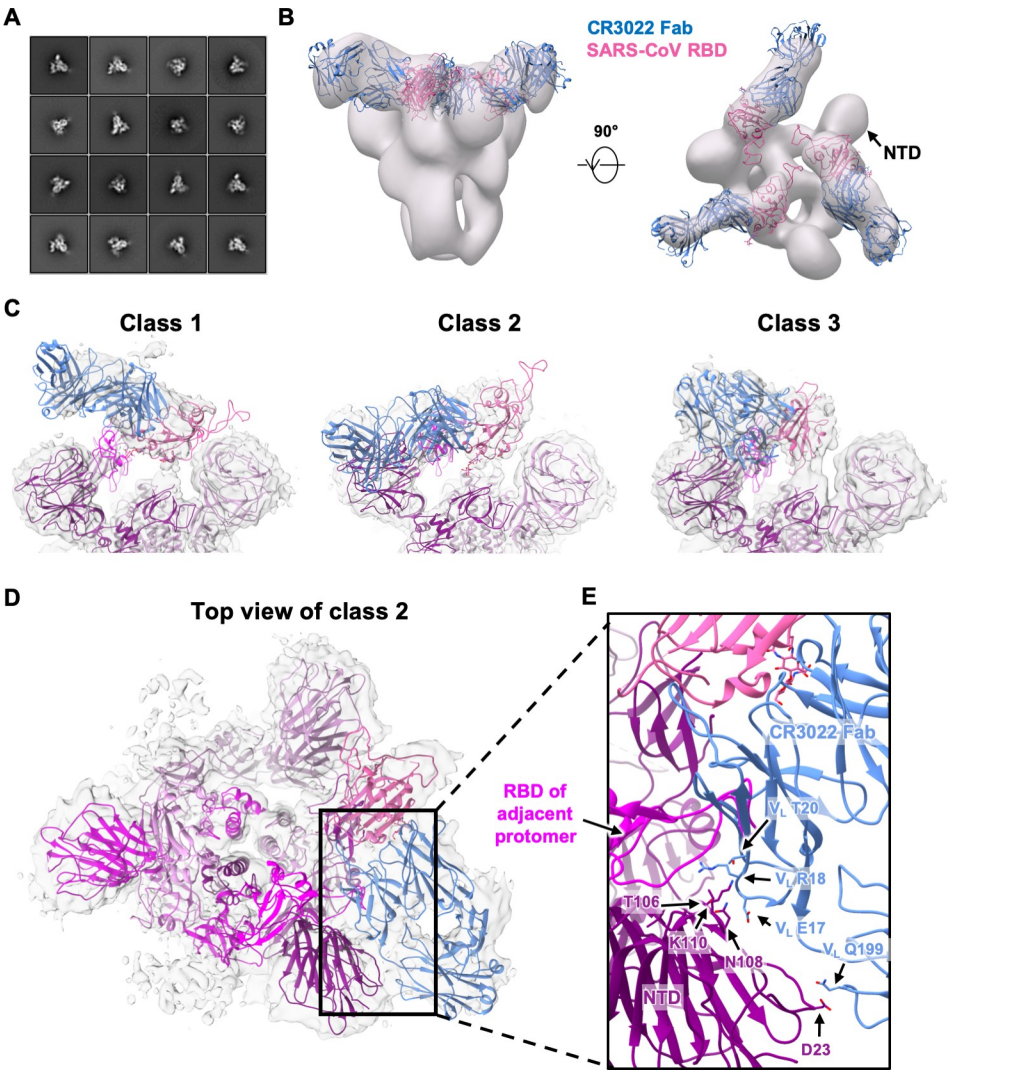

Fig 5. Negative-stain EM and cryo-EM analysis of SARS spike bound to CR3022 Fab. (A) Representative 2D nsEM class averages of the trimeric SARS-CoV spike glycoprotein complexed with three CR3022 Fabs. **(B)** Side and top view of the 3D reconstruction showing CR3022 Fabs bound to all 3 RBDs on the SARS-CoV spike. The SARS-CoV RBD-CR3022 complex from the crystal structure is fitted into the nsEM density with the RBD shown in pink and CR3022 Fab in blue. **(C)** Side views of the B-factor-sharpened cryo-EM maps (transparent gray surface representation) representing three different classes of SARS spike with CR3022 Fab with different RBD-Fab orientations. While four different classes were identified, only three classes are shown here because classes 2 and 4 are very similar (S5 Fig). The RBD-Fab complex model is fit into the densities with the RBDs shown in pink and CR3022 Fabs represented in blue. The atomic model of the apo SARS-CoV spike (PDB 6ACD) [35] is also fit into density with one RBD removed for clarity. The protomers are colored in purple, magenta and deep magenta. **(D)** Top view of the class 2 cryo-EM map depicting potential quaternary contacts between the RBD-bound Fab and the spike NTD in this conformation. In this RBD-Fab conformation, the Fab would clash with the "down" RBD of the adjacent protomer (magenta) and, therefore, the adjacent RBD can only exist in an "up" conformation. **(E)** A close-up view of the Fab-spike interface showing the superimposition of CR3022 Fab and adjacent RBD. The residues that can contribute to quaternary interactions between CR3022 light chain and the NTD in two of the four classes (2 and 4) are shown.

https://doi.org/10.1371/journal.ppat.1009089.g005

RBD flexibility and quaternary interactions in CR3022-bound SARS-CoV S protein

To address some of these issues, we performed cryo-EM analysis to interrogate the binding of CR3022 to SARS-CoV S protein at higher resolution (S4 Fig and S2 Table). Focused 3D

classification yielded 4 different structural classes with classes 2 and 4 being nearly identical at the given resolution (Figs 5C and S5). Class 3 is the most similar to the model from nsEM, although the total particle number for classes 2 and 4 together exceed that for class 3 (S5 Fig). In contrast, class 1 is the least represented. In classes 2 and 4, CR3022 also appears to make quaternary contacts with the NTD, as suggested by well-defined density in the CR3022-NTD interface (Fig 5C). The moderate resolution (6 to 7 Å) of the reconstructions precludes atomic-level descriptions, but the framework region of the CR3022 light chain in classes 2 and 4 is in close proximity to a loop region in NTD corresponding to residues 106–110. In addition, the constant region of CR3022 appears to contact residue D23 of NTD. Another notable observation is that the Fab in class 2 and 4 would clash with the adjacent RBD if it were in the "down" conformation. So, for the Fab to exist in this quaternary conformation, the adjacent RBD has to be in the "up" conformation. To evaluate the different dispositions of the RBD in these structures, we compared the cryo-EM structure of an apo form of the SARS-CoV S protein where one RBD is the "up" conformation (PDB 6ACD) [35]. The RBD in classes 1 to 4 are rotated by 84.1˚, 54.3˚, -54.7˚, and 53.7˚, respectively, relative to the apo one-up conformation (see Materials and Methods). Furthermore, the CR3022-bound RBD in class 2 and 4 is more open than in the apo form (S6 Fig), demonstrating the rotational flexibility of the RBD. In fact, RBD conformational flexibility has also been noted in an ACE2-bound SARS-CoV S protein. Three different dispositions (1 to 3) of the RBD were observed in ACE2-bound SARS-CoV S protein with RBD tilts relative to horizontal top surface of the S trimer of 51.2˚, 73.3˚ and 111.6˚ compared to 68.9˚ for the apo one-up structure [35]. Our classes 2 and 4 appear to be somewhat intermediate between dispositions 2 and 3 (S7 Fig), whereas the other classes differ from the RBD dispositions in the ACE2-bound SARS-CoV S structures. Overall, these structural analyses indicate that RBD rotational flexibility and acquisition of quaternary interactions can play an important role in CR3022 interaction with the S protein. CR3022 adds to the growing list of neutralization antibodies that can utilize quaternary interactions for binding to the S protein [12,36].

Despite the flexibility of CR3022-bound RBD, bivalent binding of CR3022 to S protein does not seem to occur on the virus surface since an IgG avidity effect was not observed in the neutralization assay (see above, Fig 2).

Discussion

While it is now known that SARS-CoV and SARS-CoV-2 differ in antigenicity despite relatively high sequence conservation [1,3,4,14], there is a paucity of understanding of the underlying molecular determinants of these antigenic changes and the structural consequences of these differences. Through structural analysis of the CR3022-RBD complex and mutagenesis experiments, we show that a single amino-acid substitution at residue 384 contributes to an important antigenic difference in a highly conserved (neutralizing) epitope between SARS--CoV-2 and SARS-CoV.

While CR3022 cannot neutralize SARS-CoV-2 WT in almost all studies [3,5,20,22], it can neutralize the SARS-CoV-2 P384A mutant. The K_D of CR3022 Fab to SARS-CoV-2 WT RBD is 68 nM, whereas to SARS-CoV-2 P384A RBD is 1 nM (Fig 1B and 1C), indicating that the affinity threshold for neutralization of SARS-CoV-2 to this epitope is in the low nM range. However, despite having a low nM affinity to SARS-CoV-2 P384A RBD, CR3022 only weakly neutralizes SARS-CoV-2 P384A with an IC_{50} of 3.2 μg/ml and SARS-CoV with an IC_{50} of 5.2 μg/ml. In contrast, antibodies with similar or less Fab binding affinity to other RBD epitopes, such as the receptor binding motif, can neutralize SARS-CoV-2 much more efficiently. For example, previously characterized SARS-CoV-2 antibodies CC12.1 and CC12.3, which

have a K_D of 17 nM and 14 nM to SARS-CoV-2 RBD, respectively, neutralize SARS-CoV-2 at an IC_{50} of ~20 ng/ml [3,37]. Of note, the K_D and IC_{50} of CC12.1 and CC12.3 were measured in the same manner as this study. The lack of correlation between affinity and neutralizing activity is therefore not due to the difference in the assays between studies. In fact, a previous study also demonstrated a lack of correlation between RBD binding and neutralization for monoclonal antibodies [3]. Together, these observations suggest that the affinity threshold for SARS--CoV-2 neutralization is different for different RBD-targeting antibodies.

The difference in affinity threshold for different epitopes is likely to be related not only in the ability to block ACE2-binding [3,38], but also in antibody avidity where bivalent binding can cross-link different RBD domains on the same or different spikes and, hence, substantially enhance binding and neutralization [23,39]. Since we first reported the structure of CR3022 in complex with SARS-CoV-2 RBD [20], multiple cross-neutralizing antibodies, including COVA1-16 [39], EY6A [17], H014 [40], and ADI-56046 [6], have been shown to bind epitopes that largely overlap with the CR3022 epitope. One of these antibodies, COVA1-16, has a strong IgG avidity effect in the neutralization assay in contrast to CR3022 [39]. Such a drastic difference in IgG avidity between CR3022 and COVA1-16 may be due to their very different angles of approach in binding to RBD, which may in turn accommodate bivalent binding of IgG COVA1-16 but not CR3022 (S8 Fig). As IgG avidity continues to emerge as an explanation for the observed potency of SARS-CoV-2 neutralizing antibodies often with little to no somatic mutations [41], future studies should investigate which epitopes and antibody approach angles give rise to avidity to the spike protein on the virus.

Given the scale of the outbreak, SARS-CoV-2 may persist and circulate in humans for years to come [42]. A number of SARS-CoV-2 vaccine candidates are currently under clinical trials (https://clinicaltrials.gov/ct2/who_table) [43], which offer a potential solution to alleviate the global health and socio-economic devastation bought by SARS-CoV-2. However, whether SARS-CoV-2 can escape vaccine-induced immunity through antigenic drift remains to be determined, although escape mutations to many monoclonal antibodies have been tested *in vitro* [2]. Identification of the key residues that are responsible for differences in antigenicity among SARS-CoV-2, SARS-CoV, and possibly other SARS-related viruses, should provide a starting point to understand the potential for antigenic drift in SARS-like coronaviruses. The ongoing efforts in SARS-CoV-2 antibody discovery and structural characterization will therefore advance our molecular understanding of antigenic variation in SARS-like CoVs, and consequences for vaccine and therapeutic design, especially to cross-neutralizing epitopes, which could aid in protection against future epidemics or pandemics.

Materials and methods

Expression and purification of RBD

RBD (residues 319–541) of the SARS-CoV-2 spike protein (GenBank: QHD43416.1) and RBD (residues: 306–527) of the SARS-CoV spike (S) protein (GenBank: ABF65836.1) were fused with an N-terminal gp67 signal peptide and a C-terminal His_6 tag, and cloned into a customized pFastBac vector [44]. Recombinant bacmid DNA was generated using the Bac-to-Bac system (Thermo Fisher Scientific). Baculovirus was generated by transfecting purified bacmid DNA into Sf9 cells using FuGENE HD (Promega), and subsequently used to infect suspension cultures of High Five cells (Thermo Fisher Scientific) at an MOI of 5 to 10. Infected High Five cells were incubated at 28˚C with shaking at 110 r.p.m. for 72 h for protein expression. The supernatant was then concentrated using a 10 kDa MW cutoff Centramate cassette (Pall Corporation). For the binding study, constructs were cloned into phCMV3 and transiently transfected into Expi293F cells using ExpiFectamine 293 Reagent (Thermo Fisher Scientific)

according to the manufacturer's instructions. The supernatant was collected at 7 days post-transfection. The RBD proteins were purified by Ni-NTA, followed by size exclusion chromatography, and buffer exchanged into 20 mM Tris-HCl pH 7.4 and 150 mM NaCl.

Expression and purification of SARS-CoV spike

The SARS-CoV spike construct (Tor2 strain) for recombinant spike protein expression contains the mammalian-codon-optimized gene encoding residues 1–1190 of the spike followed by a C-terminal T4 fibritin trimerization domain, a HRV3C cleavage site, 8x-His tag and a Twin-strep tags subcloned into the eukaryotic-expression vector pαH. Residues at 968 and 969 were replaced by prolines for generating stable spike proteins as described previously [28]. The spike plasmid was transfected into FreeStyle 293F cells and cultures were harvested at 6-day post-transfection. Proteins were purified from the supernatants on His-Complete columns using a 250 mM imidazole elution buffer. The elution was buffer exchanged to Tris-NaCl buffer (25 mM Tris, 500 mM NaCl, pH 7.4) before further purification using Superose 6 increase 10/300 column (GE Healthcare). Protein fractions corresponding to the trimeric spike proteins were collected and concentrated.

Expression and purification of CR3022 Fab

The CR3022 Fab heavy (GenBank: DQ168569.1) and light (GenBank: DQ168570.1) chains were cloned into phCMV3. The plasmids were transiently co-transfected into Expi293F cells at a ratio of 2:1 (HC:LC) using ExpiFectamine 293 Reagent (Thermo Fisher Scientific) according to the manufacturer's instructions. The supernatant was collected at 7 days post-transfection. The Fab was purified with a CaptureSelect CH1-XL Pre-packed Column (Thermo Fisher Scientific) followed by size exclusion chromatography. For crystallization, a VSRRLP variant of the elbow region was used to reduce the conformational flexibility between the Fab constant and variable domains [25].

Crystallization and structural determination

Purified CR3022 Fab with a VSRRLP modification in the elbow region and SARS-CoV RBD were mixed at a molar ratio of 1:1 and incubated overnight at 4˚C. The complex (7.5 mg/ml) was screened for crystallization using the 384 conditions of the JCSG Core Suite (Qiagen) on our custom-designed robotic CrystalMation system (Rigaku) at Scripps Research by the vapor diffusion method in sitting drops containing 0.1 μl of protein and 0.1 μl of reservoir solution. Optimized crystals were then grown in 2 M sodium chloride and 10% PEG 6000 at 4˚C. Crystals were grown for 7 days and then flash cooled in liquid nitrogen. Diffraction data were collected at cryogenic temperature (100 K) at Stanford Synchrotron Radiation Lightsource (SSRL) beamline 12–2 with a wavelength of 1.033 Å, and processed with HKL2000 [45]. Structures were solved by molecular replacement using PHASER [46] with PDB 6W41 for CR3022 Fab [20] and PDB 2AJF for SARS--CoV RBD [47]. Iterative model building and refinement were carried out in COOT [48] and PHENIX [49], respectively. Ramachandran statistics were calculated using MolProbity [50].

Construction of individual mutants

Individual mutants for validation experiments were constructed using the QuikChange XL Mutagenesis kit (Stratagene) according to the manufacturer's instructions.

Negative-stain electron microscopy

Six molar excess of CR3022 Fab (unmodified) was added to SARS-CoV spike protein 1 hour prior to direct deposition onto carbon-coated 400-mesh copper grids. The grids were stained

with 2% (w/v) uranyl-formate for 90 seconds immediately following sample application. Grids were imaged on Tecnai T12 Spirit at 120 keV with a 4k x 4k Eagle CCD. Micrographs were collected using Leginon [51] and images were transferred to Appion [52] for particle picking using a difference-of-Gaussians picker (DoG-picker) [53] and generation of particle stacks. Particle stacks were further transferred to Relion [54] for 2D classification followed by 3D classification to select good classes. Select 3D classes were auto-refined on Relion and used for making figures using UCSF Chimera [55].

Cryo-EM sample preparation

SARS-CoV spike protein was incubated with six molar excess of CR3022 Fab for 2 h. 3.5 μL of the complex (0.9 mg/ml) was mixed with 0.5 μL of 0.04 mM lauryl maltose neopentyl glycol (LMNG) solution immediately before sample deposition onto a 1.2/1.3 300-Gold grid (EMS). The grids were plasma cleaned for 7 seconds using a Gatan Solarus 950 Plasma system prior to sample deposition. Following sample application, grids were blotted for 3 seconds before being vitrified in liquid ethane using a Vitrobot Mark IV (Thermo Fisher).

Cryo-EM data collection and processing

Data collection was performed using a Talos Arctica TEM at 200 kV with a Gatan K2 Summit detector at a magnification of 36,000x, resulting in a 1.15 Å pixel size. Total exposure was split into 250 ms frames with a total cumulative dose of $\sim$50 $e^-/Å^2$. Micrographs were collected through Leginon software at a nominal defocus range of -0.4 μm to -1.6 μm and MotionCor2 was used for alignment and dose weighting of the frames [51,56]. Micrographs were transferred to CryoSPARC 2.9 for further processing [57]. CTF estimations were performed using GCTF and micrographs were selected using the Curate Exposures tool in CryoSPARC based on their CTF resolution estimates (cutoff 5 Å) for downstream particle picking, extraction and iterative rounds of 2D classification and selection [58]. Particles selected from 2D classes were transferred to Relion 3.1 for direct C3 refinement, symmetry expansion of particles and iterative rounds of 3D focused classification using spherical masks around the RBD and Fab [54]. Final subsets of clean particles from 4 different classes were each refined with C1 symmetry. Figures were generated using UCSF Chimera and UCSF Chimera X [55].

Calculation of rotation angles

Comparisons of subunit rotation angles among different structures were performed with a software 'Superpose' in the CCP4 package [59,60]. For each classified conformation, the Cα atoms of the RBD domain are superimposed to the equivalent atoms of the RBD in "up"-conformation in a previously reported spike trimer cryo-EM structure (PDB 6ACD) [35]. The rotation matrices generated by superposing each pair of structures with 'Superpose' were adopted to calculate the subunit rotation angle following the equation shown as below:

$$\theta = \cos^{-1}\frac{X_{11} + Y_{22} + Z_{33} - 1}{2}$$

where θ is the subunit rotation angle, X_{11}, Y_{22}, and Z_{33} represent the X_{11}, Y_{22}, and Z_{33} values in the rotation matrix calculated for the superpose.

Biolayer interferometry binding assay

Binding assays were performed by biolayer interferometry (BLI) using an Octet Red instrument (FortéBio) as described previously [61]. Briefly, His_6-tagged RBD proteins at 20 to

100 μg/ml in 1x kinetics buffer (1x PBS, pH 7.4, 0.01% BSA and 0.002% Tween 20) were loaded onto Anti-Penta-HIS (HIS1K) biosensors and incubated with the indicated concentrations of CR3022 Fab. The assay consisted of five steps: 1) baseline: 60 s with 1x kinetics buffer; 2) loading: 300 s with His_6-tagged S or RBD proteins; 3) baseline: 60 s with 1x kinetics buffer; 4) association: 120 s with samples (Fab or IgG); and 5) dissociation: 120 s with 1x kinetics buffer. For estimating the exact K_D, a 1:1 binding model was used.

Pseudovirus neutralization assay

Pseudovirus preparation and assay were performed as previously described [3]. Briefly, MLV-gag/pol and MLV-CMV plasmids was co-transfected into HEK293T cells along with full-length or P384A SARS-CoV-2 spike plasmids using Lipofectamine 2000 to produce pseudoviruses competent for single-round infection. The supernatant containing MLV-pseudotyped viral particles was collected at 48 hours post transfection, aliquoted and frozen at -80˚C until used. For each well in a 96-well half-area plate, 25 μl of virus was immediately mixed with 25 μl of serially diluted IgG or Fab, and incubated for 1 hour at 37˚C. For each well, 10,000 HeLa-hACE2 cells in 50 μl of media supplemented with 20 μg/ml dextran were added to the antibody-virus mixture. The 96-well half-area plate was then incubated at 37˚C. At 42 to 48 hours post-infection, HeLa-hACE2 cells were lysed using 1x luciferase lysis buffer (25 mM Gly-Gly pH 7.8, 15 mM $MgSO_4$, 4 mM EGTA, and 1% Triton X-100). Luciferase intensity was then measured using Bright-Glo Luciferase Assay System (Promega) according to the manufacturer's instructions. Percentage of neutralization was calculated using the following equation:

$$\%\ neutralization = 100 \times \left(1 - \frac{RULs\ of\ sample - Average\ RULs\ of\ Background}{Average\ of\ RULs\ of\ Virus\ only\ control - Average\ RULs\ of\ Backgroud}\right)$$

Phylogenetic tree construction

RBD protein sequences from SARS-CoV-2, SARS-CoV, and SARS-related coronavirus (SARSr-CoV) strains were retrieved from the following accession codes:

- GenBank QHD43416.1 (SARS-CoV-2)
- GenBank ABF65836.1 (SARS-CoV)
- GenBank AID16716.1 (Bat SARSr-CoV Longquan-140)
- GenBank AAY88866.1 (Bat SARSr-CoV HKU3-1)
- GenBank AIA62320.1 (Bat SARSr-CoV GX2013)
- GenBank AIA62310.1 (Bat SARSr-CoV HuB2013)
- GenBank ACU31032.1 (Bat SARSr-CoV Rs672)
- GenBank AAZ67052.1 (Bat SARSr-CoV Rp3)
- GenBank AIA62300.1 (Bat SARSr-CoV SX2013)
- GenBank ABD75323.1 (Bat SARSr-CoV Rf1)
- GenBank AVP78031.1 (Bat SARSr-CoV ZC45)
- GenBank AVP78042.1 (Bat SARSr-CoV ZXC21)
- GISAID EPI_ISL_410721 (Pangolin BetaCoV Guandong2019)

- GenBank QHR63300.2 (Bat CoV RaTG13)
- NCBI Reference Sequence YP_003858584.1 (Bat SARSr-CoV BM48-31)
- GenBank ALK02457.1 (Bat SARSr-CoV WIV16)
- GenBank AGZ48828.1 (Bat SARSr-CoV WIV1)

Multiple sequence alignment of the RBD sequences was performed by MUSCLE version 3.8.31 [62]. Phylogenetic tree was generated by FastTree version 2.1.8 [63] and displayed by FigTree version 1.4.2 (http://tree.bio.ed.ac.uk/software/figtree/).

Supporting information

S1 Fig. Phylogenetic tree of S proteins from SARS-CoV-2, SARS-CoV, and SARS-related coronavirus (SARSr-CoV) strains. Branches corresponding to strains that have A384 are colored in red on the phylogenetic tree. Scale bar represents 0.05 amino-acid substitutions per position.
(PDF)

S2 Fig. X-ray electron density maps for epitope and paratope regions of SARS-CoV RBD with Fab CR3022. (A) Final 2Fo-Fc electron density maps for the side chains in the epitope region of SARS-CoV-2 contoured at 1 σ. **(B)** Final 2Fo-Fc electron density maps for the paratope region of CR3022 contoured at 1 σ. The heavy chain is colored in orange, and light chain in yellow. Epitope and paratope residues are labeled.
(PDF)

S3 Fig. Structural alignment of CR3022-bound SARS-CoV RBD and CR3022-bound SARS-CoV-2 RBD. Structure of CR3022 in complex with SARS-CoV RBD (this study) is aligned to that with SARS-CoV-2 RBD (PDB 6W41). Structural alignment was performed using CR3022 heavy chain variable domain. Red: CR3022 in complex with SARS-CoV RBD. Blue: CR3022 in complex with SARS-CoV-2 RBD.
(PDF)

S4 Fig. Representative cryo-electron micrograph and 2D class averages of the SARS-CoV spike in complex with CR3022 Fab. The top panel shows a representative cryo-electron micrograph of the SARS-CoV spike complexed with CR3022 Fab, whereas the bottom panels show the 2D class averages.
(PDF)

S5 Fig. Workflow for cryo-EM data processing. Four 3D class averages of complex of the SARS-CoV spike and CR3022 were found during data processing.
(PDF)

S6 Fig. Comparison of conformations of CR3022-bound and unbound RBDs. The conformation of CR3022-bound RBD in class 2 and 4 is compared to the conformation of RBD on an unliganded SARS-CoV S protein (PDB 6ACD) [35].
(PDF)

S7 Fig. Comparison of conformations of CR3022-bound and ACE2-bound RBDs. The conformation of CR3022-bound RBD in class 2 and 4 is compared to that of dispositions 2 and 3 of ACE2-bound RBD (PDB 6ACJ and 6ACK, respectively) [35].
(PDF)

S8 Fig. Comparison of the angles of approach of CR3022 and COVA1-16 to RBD. The angles of approach of CR3022 (blue) and COVA1-16 (wheat, PDB 7JMW) [39] to RBD are compared. Receptor-binding motif (residues 472–498) on the RBD is colored in pink.
(PDF)

S1 Table. X-ray data collection and refinement statistics.
(PDF)

S2 Table. Cryo-EM data collection and refinement statistics.
(PDF)

Acknowledgments

We thank Henry Tien for technical support with the crystallization robot, Jeanne Matteson for contribution to mammalian cell culture, Wenli Yu to insect cell culture, Robyn Stanfield for assistance in data collection, and Chris Mok for pilot testing of the pseudovirus assay. We are grateful to the staff of Stanford Synchrotron Radiation Laboratory (SSRL) Beamline 12–2 for assistance.

Author Contributions

Conceptualization: Nicholas C. Wu, Meng Yuan, Ian A. Wilson.

Data curation: Nicholas C. Wu, Meng Yuan, Ian A. Wilson.

Formal analysis: Nicholas C. Wu, Meng Yuan.

Funding acquisition: Nicholas C. Wu, Dennis R. Burton, David Nemazee, Andrew B. Ward, Ian A. Wilson.

Investigation: Nicholas C. Wu, Meng Yuan, Sandhya Bangaru, Deli Huang, Xueyong Zhu, Chang-Chun D. Lee, Hannah L. Turner, Linghang Peng, Linlin Yang.

Methodology: Nicholas C. Wu, Meng Yuan.

Resources: Dennis R. Burton, David Nemazee, Andrew B. Ward, Ian A. Wilson.

Supervision: Andrew B. Ward, Ian A. Wilson.

Validation: Nicholas C. Wu, Meng Yuan, Sandhya Bangaru, Deli Huang.

Visualization: Nicholas C. Wu, Meng Yuan, Sandhya Bangaru, Deli Huang.

Writing – original draft: Nicholas C. Wu, Meng Yuan, Sandhya Bangaru, Deli Huang, Andrew B. Ward, Ian A. Wilson.

Writing – review & editing: Nicholas C. Wu, Meng Yuan, Sandhya Bangaru, Deli Huang, Xueyong Zhu, Chang-Chun D. Lee, Hannah L. Turner, Linghang Peng, Linlin Yang, Dennis R. Burton, David Nemazee, Andrew B. Ward, Ian A. Wilson.

References

1. Brouwer PJM, Caniels TG, van der Straten K, Snitselaar JL, Aldon Y, Bangaru S, et al. Potent neutralizing antibodies from COVID-19 patients define multiple targets of vulnerability. Science. 2020; 369 (6504):643–50. https://doi.org/10.1126/science.abc5902 PMID: 32540902
2. Baum A, Fulton BO, Wloga E, Copin R, Pascal KE, Russo V, et al. Antibody cocktail to SARS-CoV-2 spike protein prevents rapid mutational escape seen with individual antibodies. Science. 2020; 369 (6506):1014–8. Epub 2020/06/17. https://doi.org/10.1126/science.abd0831 PMID: 32540904; PubMed Central PMCID: PMC7299283.

3. Rogers TF, Zhao F, Huang D, Beutler N, Burns A, He W-t, et al. Isolation of potent SARS-CoV-2 neutralizing antibodies and protection from disease in a small animal model. Science. 2020; 369 (6506):956–63. https://doi.org/10.1126/science.abc7520 PMID: 32540903
4. Ju B, Zhang Q, Ge J, Wang R, Sun J, Ge X, et al. Human neutralizing antibodies elicited by SARS-CoV-2 infection. Nature. 2020; 584(7819):115–9. Epub 2020/05/27. https://doi.org/10.1038/s41586-020-2380-z PMID: 32454513.
5. Chi X, Yan R, Zhang J, Zhang G, Zhang Y, Hao M, et al. A neutralizing human antibody binds to the N-terminal domain of the Spike protein of SARS-CoV-2. Science. 2020; 368(6504):1274–8. https://doi.org/10.1126/science.abc6952 PMID: 32571838
6. Wec AZ, Wrapp D, Herbert AS, Maurer D, Haslwanter D, Sakharkar M, et al. Broad neutralization of SARS-related viruses by human monoclonal antibodies. Science. 2020; 369(6504):731–6. https://doi.org/10.1126/science.abc7424 PMID: 32540900
7. Pinto D, Park YJ, Beltramello M, Walls AC, Tortorici MA, Bianchi S, et al. Cross-neutralization of SARS-CoV-2 by a human monoclonal SARS-CoV antibody. Nature. 2020; 583(7815):290–5. Epub 2020/05/19. https://doi.org/10.1038/s41586-020-2349-y PMID: 32422645.
8. Zost SJ, Gilchuk P, Case JB, Binshtein E, Chen RE, Nkolola JP, et al. Potently neutralizing and protective human antibodies against SARS-CoV-2. Nature. 2020; 584(7821):443–9. Epub 2020/07/16. https://doi.org/10.1038/s41586-020-2548-6 PMID: 32668443.
9. Cao Y, Su B, Guo X, Sun W, Deng Y, Bao L, et al. Potent neutralizing antibodies against SARS-CoV-2 identified by high-throughput single-cell sequencing of convalescent patients' B cells. Cell. 2020; 182 (1):73–84. Epub 2020/05/20. https://doi.org/10.1016/j.cell.2020.05.025 PMID: 32425270; PubMed Central PMCID: PMC7231725.
10. Seydoux E, Homad LJ, MacCamy AJ, Parks KR, Hurlburt NK, Jennewein MF, et al. Analysis of a SARS-CoV-2-infected individual reveals development of potent neutralizing antibodies with limited somatic mutation. Immunity. 2020; 53(1):98–105. https://doi.org/10.1016/j.immuni.2020.06.001 PMID: 32561270
11. Shi R, Shan C, Duan X, Chen Z, Liu P, Song J, et al. A human neutralizing antibody targets the receptor binding site of SARS-CoV-2. Nature. 2020; 584(7819):120–4. Epub 2020/05/27. https://doi.org/10.1038/s41586-020-2381-y PMID: 32454512.
12. Liu L, Wang P, Nair MS, Yu J, Rapp M, Wang Q, et al. Potent neutralizing antibodies directed to multiple epitopes on SARS-CoV-2 spike. Nature. 2020; 584(7821):450–6. Epub 2020/07/23. https://doi.org/10.1038/s41586-020-2571-7 PMID: 32698192.
13. Zhou P, Yang XL, Wang XG, Hu B, Zhang L, Zhang W, et al. A pneumonia outbreak associated with a new coronavirus of probable bat origin. Nature. 2020; 579(7798):270–3. Epub 2020/02/06. https://doi.org/10.1038/s41586-020-2012-7 PMID: 32015507.
14. Lv H, Wu NC, Tsang OT-Y, Yuan M, Perera RAPM, Leung WS, et al. Cross-reactive antibody response between SARS-CoV-2 and SARS-CoV infections. Cell Rep. 2020; 31(9):107725. https://doi.org/10.1016/j.celrep.2020.107725 PMID: 32426212
15. Ou X, Liu Y, Lei X, Li P, Mi D, Ren L, et al. Characterization of spike glycoprotein of SARS-CoV-2 on virus entry and its immune cross-reactivity with SARS-CoV. Nat Commun. 2020; 11(1):1620. Epub 2020/03/30. https://doi.org/10.1038/s41467-020-15562-9 PMID: 32221306; PubMed Central PMCID: PMC7100515.
16. Wang C, Li W, Drabek D, Okba NMA, van Haperen R, Osterhaus ADME, et al. A human monoclonal antibody blocking SARS-CoV-2 infection. Nat Commun. 2020; 11(1):2251. https://doi.org/10.1038/s41467-020-16256-y PMID: 32366817
17. Zhou D, Duyvesteyn HME, Chen C-P, Huang C-G, Chen T-H, Shih S-R, et al. Structural basis for the neutralization of SARS-CoV-2 by an antibody from a convalescent patient. Nat Struct Mol Biol. 2020; 27:950–8. https://doi.org/10.1038/s41594-020-0480-y PMID: 32737466
18. ter Meulen J, van den Brink EN, Poon LL, Marissen WE, Leung CS, Cox F, et al. Human monoclonal antibody combination against SARS coronavirus: synergy and coverage of escape mutants. PLoS Med. 2006; 3(7):e237. Epub 2006/06/27. https://doi.org/10.1371/journal.pmed.0030237 PMID: 16796401; PubMed Central PMCID: PMC1483912.
19. Tian X, Li C, Huang A, Xia S, Lu S, Shi Z, et al. Potent binding of 2019 novel coronavirus spike protein by a SARS coronavirus-specific human monoclonal antibody. Emerg Microbes Infect. 2020; 9(1):382–5. Epub 2020/02/18. https://doi.org/10.1080/22221751.2020.1729069 PMID: 32065055.
20. Yuan M, Wu NC, Zhu X, Lee CD, So RTY, Lv H, et al. A highly conserved cryptic epitope in the receptor-binding domains of SARS-CoV-2 and SARS-CoV. Science. 2020; 368(6491):630–3. Epub 2020/04/05. https://doi.org/10.1126/science.abb7269 PMID: 32245784.

21. Liu H, Wu NC, Yuan M, Bangaru S, Torres JL, Caniels TG, et al. Cross-neutralization of a SARS-CoV-2 antibody to a functionally conserved site is mediated by avidity. bioRxiv. https://doi.org/10.1101/2020.08.02.233536 PMID: 32793906

22. Yi C, Sun X, Ye J, Ding L, Liu M, Yang Z, et al. Key residues of the receptor binding motif in the spike protein of SARS-CoV-2 that interact with ACE2 and neutralizing antibodies. Cell Mol Immunol. 2020; 17 (6):621–30. Epub 2020/05/18. https://doi.org/10.1038/s41423-020-0458-z PMID: 32415260; PubMed Central PMCID: PMC7227451.

23. Barnes CO, West AP, Huey-Tubman KE, Hoffmann MAG, Sharaf NG, Hoffman PR, et al. Structures of human antibodies bound to SARS-CoV-2 spike reveal common epitopes and recurrent features of antibodies. Cell. 2020; 182(4):828–42. https://doi.org/10.1016/j.cell.2020.06.025 PMID: 32645326

24. Li W, Shi Z, Yu M, Ren W, Smith C, Epstein JH, et al. Bats are natural reservoirs of SARS-like coronaviruses. Science. 2005; 310(5748):676–9. Epub 2005/10/01. https://doi.org/10.1126/science.1118391 PMID: 16195424.

25. Bailey LJ, Sheehy KM, Dominik PK, Liang WG, Rui H, Clark M, et al. Locking the elbow: improved antibody Fab fragments as chaperones for structure determination. J Mol Biol. 2018; 430(3):337–47. Epub 2017/12/24. https://doi.org/10.1016/j.jmb.2017.12.012 PMID: 29273204; PubMed Central PMCID: PMC5800945.

26. Gui M, Song W, Zhou H, Xu J, Chen S, Xiang Y, et al. Cryo-electron microscopy structures of the SARS-CoV spike glycoprotein reveal a prerequisite conformational state for receptor binding. Cell Res. 2017; 27(1):119–29. Epub 2016/12/23. https://doi.org/10.1038/cr.2016.152 PMID: 28008928; PubMed Central PMCID: PMC5223232.

27. Yuan Y, Cao D, Zhang Y, Ma J, Qi J, Wang Q, et al. Cryo-EM structures of MERS-CoV and SARS-CoV spike glycoproteins reveal the dynamic receptor binding domains. Nat Commun. 2017; 8:15092. Epub 2017/04/11. https://doi.org/10.1038/ncomms15092 PMID: 28393837; PubMed Central PMCID: PMC5394239.

28. Kirchdoerfer RN, Wang N, Pallesen J, Wrapp D, Turner HL, Cottrell CA, et al. Stabilized coronavirus spikes are resistant to conformational changes induced by receptor recognition or proteolysis. Sci Rep. 2018; 8(1):15701. Epub 2018/10/26. https://doi.org/10.1038/s41598-018-34171-7 PMID: 30356097; PubMed Central PMCID: PMC6200764.

29. Huo J, Zhao Y, Ren J, Zhou D, Duyvesteyn HME, Ginn HM, et al. Neutralization of SARS-CoV-2 by destruction of the prefusion spike. Cell Host Microbe. 2020; 28(3):445–54. Epub 2020/06/26. https://doi.org/10.1016/j.chom.2020.06.010 PMID: 32585135; PubMed Central PMCID: PMC7303615.

30. Wrapp D, Wang N, Corbett KS, Goldsmith JA, Hsieh CL, Abiona O, et al. Cryo-EM structure of the 2019-nCoV spike in the prefusion conformation. Science. 2020; 367(6483):1260–3. Epub 2020/02/23. https://doi.org/10.1126/science.abb2507 PMID: 32075877.

31. Walls AC, Park YJ, Tortorici MA, Wall A, McGuire AT, Veesler D. Structure, function, and antigenicity of the SARS-CoV-2 spike glycoprotein. Cell. 2020; 181(2):281–92.e6. Epub 2020/03/11. https://doi.org/10.1016/j.cell.2020.02.058 PMID: 32155444.

32. Cai Y, Zhang J, Xiao T, Peng H, Sterling SM, Walsh RM Jr., et al. Distinct conformational states of SARS-CoV-2 spike protein. Science. 2020; 369(6511):1586–92. Epub 2020/07/23. https://doi.org/10.1126/science.abd4251 PMID: 32694201.

33. Ke Z, Oton J, Qu K, Cortese M, Zila V, McKeane L, et al. Structures and distributions of SARS-CoV-2 spike proteins on intact virions. Nature. 2020. https://doi.org/10.1038/s41586-020-2665-2 PMID: 32805734

34. Yao H, Song Y, Chen Y, Wu N, Xu J, Sun C, et al. Molecular architecture of the SARS-CoV-2 virus. Cell. 2020; 183(3):730–738.e13 Epub 2020/09/06. https://doi.org/10.1016/j.cell.2020.09.018 PMID: 32979942; PubMed Central PMCID: PMC7474903.

35. Song W, Gui M, Wang X, Xiang Y. Cryo-EM structure of the SARS coronavirus spike glycoprotein in complex with its host cell receptor ACE2. PLoS Pathog. 2018; 14(8):e1007236. Epub 2018/08/14. https://doi.org/10.1371/journal.ppat.1007236 PMID: 30102747; PubMed Central PMCID: PMC6107290.

36. Barnes CO, Jette CA, Abernathy ME, Dam KA, Esswein SR, Gristick HB, et al. SARS-CoV-2 neutralizing antibody structures inform therapeutic strategies. Nature. 2020. Epub 2020/10/13. https://doi.org/10.1038/s41586-020-2852-1 PMID: 33045718.

37. Yuan M, Liu H, Wu NC, Lee C-CD, Zhu X, Zhao F, et al. Structural basis of a shared antibody response to SARS-CoV-2. Science. 2020; 369(6507):1119–23. https://doi.org/10.1126/science.abd2321 PMID: 32661058; PubMed Central PMCID: PMC716439.

38. Tan CW, Chia WN, Qin X, Liu P, Chen MI, Tiu C, et al. A SARS-CoV-2 surrogate virus neutralization test based on antibody-mediated blockage of ACE2-spike protein-protein interaction. Nat Biotechnol. 2020; 38:1073–8. Epub 2020/07/25. https://doi.org/10.1038/s41587-020-0631-z PMID: 32704169.

39. Liu H, Wu NC, Yuan M, Bangaru S, Torres JL, Caniels TG, et al. Cross-neutralization of a SARS-CoV-2 antibody to a functionally conserved site is mediated by avidity. Immunity. 2020. S1074-7613(20) 30464–7. Epub 2020/11/21. https://doi.org/10.1016/j.immuni.2020.10.023 PMID: 33242394. PubMedCentral PMCID: PMC7687367.

40. Lv Z, Deng YQ, Ye Q, Cao L, Sun CY, Fan C, et al. Structural basis for neutralization of SARS-CoV-2 and SARS-CoV by a potent therapeutic antibody. Science. 2020; 369(6510):1505–9. Epub 2020/07/25. https://doi.org/10.1126/science.abc5881 PMID: 32703908; PubMed Central PMCID: PMC7402622.

41. Yuan M, Liu H, Wu NC, Wilson IA. Recognition of the SARS-CoV-2 receptor binding domain by neutralizing antibodies. Biochem Biophys Res Commun. 2020. https://doi.org/10.1016/j.bbrc.2020.10.012 PMID: 33069360; PubMed Central PMCID: PMC7547570.

42. Kissler SM, Tedijanto C, Goldstein E, Grad YH, Lipsitch M. Projecting the transmission dynamics of SARS-CoV-2 through the postpandemic period. Science. 2020; 368(6493):860–8. Epub 2020/04/16. https://doi.org/10.1126/science.abb5793 PMID: 32291278; PubMed Central PMCID: PMC7164482.

43. Amanat F, Krammer F. SARS-CoV-2 vaccines: status report. Immunity. 2020; 52(4):583–9. Epub 2020/04/08. https://doi.org/10.1016/j.immuni.2020.03.007 PMID: 32259480; PubMed Central PMCID: PMC7136867.

44. Ekiert DC, Friesen RH, Bhabha G, Kwaks T, Jongeneelen M, Yu W, et al. A highly conserved neutralizing epitope on group 2 influenza A viruses. Science. 2011; 333(6044):843–50. https://doi.org/10.1126/science.1204839 PMID: 21737702; PubMed Central PMCID: PMC3210727.

45. Otwinowski Z, Minor W. Processing of X-ray diffraction data collected in oscillation mode. Methods Enzymol. 1997; 276:307–26. Epub 1997/01/01. PMID: 27754618.

46. McCoy AJ, Grosse-Kunstleve RW, Adams PD, Winn MD, Storoni LC, Read RJ. Phaser crystallographic software. J Appl Crystallogr. 2007; 40(Pt 4):658–74. https://doi.org/10.1107/S0021889807021206 PMID: 19461840; PubMed Central PMCID: PMC2483472.

47. Li F, Li W, Farzan M, Harrison SC. Structure of SARS coronavirus spike receptor-binding domain complexed with receptor. Science. 2005; 309(5742):1864–8. Epub 2005/09/17. https://doi.org/10.1126/science.1116480 PMID: 16166518.

48. Emsley P, Lohkamp B, Scott WG, Cowtan K. Features and development of Coot. Acta Crystallogr D Biol Crystallogr. 2010; 66(Pt 4):486–501. https://doi.org/10.1107/S0907444910007493 PMID: 20383002; PubMed Central PMCID: PMC2852313.

49. Adams PD, Afonine PV, Bunkoczi G, Chen VB, Davis IW, Echols N, et al. PHENIX: a comprehensive Python-based system for macromolecular structure solution. Acta Crystallogr D Biol Crystallogr. 2010; 66(Pt 2):213–21. Epub 2010/02/04. https://doi.org/10.1107/S0907444909052925 PMID: 20124702; PubMed Central PMCID: PMC2815670.

50. Chen VB, Arendall WB 3rd, Headd JJ, Keedy DA, Immormino RM, Kapral GJ, et al. MolProbity: all-atom structure validation for macromolecular crystallography. Acta Crystallogr D Biol Crystallogr. 2010; 66(Pt 1):12–21. https://doi.org/10.1107/S0907444909042073 PMID: 20057044; PubMed Central PMCID: PMC2803126.

51. Suloway C, Pulokas J, Fellmann D, Cheng A, Guerra F, Quispe J, et al. Automated molecular microscopy: the new Leginon system. J Struct Biol. 2005; 151(1):41–60. Epub 2005/05/14. https://doi.org/10.1016/j.jsb.2005.03.010 PMID: 15890530.

52. Lander GC, Stagg SM, Voss NR, Cheng A, Fellmann D, Pulokas J, et al. Appion: an integrated, database-driven pipeline to facilitate EM image processing. J Struct Biol. 2009; 166(1):95–102. https://doi.org/10.1016/j.jsb.2009.01.002 PMID: 19263523; PubMed Central PMCID: PMC2775544.

53. Voss NR, Yoshioka CK, Radermacher M, Potter CS, Carragher B. DoG Picker and TiltPicker: software tools to facilitate particle selection in single particle electron microscopy. J Struct Biol. 2009; 166 (2):205–13. https://doi.org/10.1016/j.jsb.2009.01.004 PMID: 19374019; PubMed Central PMCID: PMC2768396.

54. Zivanov J, Nakane T, Forsberg BO, Kimanius D, Hagen WJ, Lindahl E, et al. New tools for automated high-resolution cryo-EM structure determination in RELION-3. eLife. 2018; 7:e42166 Epub 2018/11/10. https://doi.org/10.7554/eLife.42166 PMID: 30412051; PubMed Central PMCID: PMC6250425.

55. Pettersen EF, Goddard TD, Huang CC, Couch GS, Greenblatt DM, Meng EC, et al. UCSF Chimera—a visualization system for exploratory research and analysis. J Comput Chem. 2004; 25(13):1605–12. Epub 2004/07/21. https://doi.org/10.1002/jcc.20084 PMID: 15264254.

56. Zheng SQ, Palovcak E, Armache JP, Verba KA, Cheng Y, Agard DA. MotionCor2: anisotropic correction of beam-induced motion for improved cryo-electron microscopy. Nat Methods. 2017; 14(4):331–2. Epub 2017/03/03. https://doi.org/10.1038/nmeth.4193 PMID: 28250466; PubMed Central PMCID: PMC5494038.

57. Punjani A, Rubinstein JL, Fleet DJ, Brubaker MA. cryoSPARC: algorithms for rapid unsupervised cryo-EM structure determination. Nat Methods. 2017; 14(3):290–6. Epub 2017/02/07. https://doi.org/10.1038/nmeth.4169 PMID: 28165473.

58. Zhang K. Gctf: Real-time CTF determination and correction. J Struct Biol. 2016; 193(1):1–12. Epub 2015/11/26. https://doi.org/10.1016/j.jsb.2015.11.003 PMID: 26592709; PubMed Central PMCID: PMC4711343.

59. Winn MD, Ballard CC, Cowtan KD, Dodson EJ, Emsley P, Evans PR, et al. Overview of the CCP4 suite and current developments. Acta Crystallogr D Biol Crystallogr. 2011; 67(Pt 4):235–42. Epub 2011/04/05. https://doi.org/10.1107/S0907444910045749 PMID: 21460441; PubMed Central PMCID: PMC3069738.

60. Krissinel E, Henrick K. Secondary-structure matching (SSM), a new tool for fast protein structure alignment in three dimensions. Acta Crystallogr D Biol Crystallogr. 2004; 60(Pt 12 Pt 1):2256–68. Epub 2004/12/02. https://doi.org/10.1107/S0907444904026460 PMID: 15572779.

61. Wu NC, Grande G, Turner HL, Ward AB, Xie J, Lerner RA, et al. In vitro evolution of an influenza broadly neutralizing antibody is modulated by hemagglutinin receptor specificity. Nat Commun. 2017; 8:15371. https://doi.org/10.1038/ncomms15371 PMID: 28504265; PubMed Central PMCID: PMC5440694.

62. Edgar RC. MUSCLE: multiple sequence alignment with high accuracy and high throughput. Nucleic Acids Res. 2004; 32(5):1792–7. Epub 2004/03/23. https://doi.org/10.1093/nar/gkh340 PMID: 15034147; PubMed Central PMCID: PMC390337.

63. Price MN, Dehal PS, Arkin AP. FastTree 2—approximately maximum-likelihood trees for large alignments. PLoS One. 2010; 5(3):e9490. Epub 2010/03/13. https://doi.org/10.1371/journal.pone.0009490 PMID: 20224823; PubMed Central PMCID: PMC2835736.